Acta Crystallographica Section D
Biological Crystallography
ISSN 0907-4449

FIP: a highly automated beamline for multiwavelength anomalous diffraction experiments

M. Roth,[a] P. Carpentier,[a] O. Kaïkati,[a] J. Joly,[a] P. Charrault,[a] M. Pirocchi,[a] R. Kahn,[b] E. Fanchon,[b] L. Jacquamet,[a] F. Borel,[a] A. Bertoni,[c] P. Israel-Gouy[a] and J.-L. Ferrer[a]*

[a]Laboratoire de Cristallographie et Cristallogenèse des Protèines (LCCP), Institut de Biologie Structurale J.-P. Ebel CEA–CNRS, 41 Rue Jules Horowitz, 38027 Grenoble CEDEX 1, France, [b]Laboratoire de Cristallographie Macromolèculaire (LCM), Institut de Biologie Structurale J.-P. Ebel CEA–CNRS, 41 Rue Jules Horowitz, 38027 Grenoble CEDEX 1, France, and [c]Institut de Biologie Structurale J.-P. Ebel CEA–CNRS, 41 Rue Jules Horowitz, 38027 Grenoble CEDEX 1, France

Correspondence e-mail: ferrer@lccp.ibs.fr

Received 28 November 2001
Accepted 28 February 2002

FIP is a French Collaborating Research Group (CRG) beamline at the European Synchrotron Radiation Facility (ESRF) dedicated exclusively to crystallography of biological macromolecules, with a special emphasis on multiwavelength anomalous diffraction data collection in the 0.7–1.81 Å wavelength range. The optics, consisting of long cylindrical grazing-angle mirrors associated with a cryocooled double-crystal monochromator, delivers an optimal beam in the corresponding energy range. The high level of automation, which includes automated crystal centring, automated data-collection management and data processing, makes the use of this beamline very easy. This is illustrated by the large number of challenging structures that have been solved since 1999.

1. Introduction

The beamline FIP (French beamline for Investigation of Proteins) is a French Collaborative Research Group (CRG) at the ESRF dedicated exclusively to the crystallography of biological macromolecules, with a special emphasis on multiwavelength anomalous diffraction (MAD) data collection. The very first tests with X-rays were carried out in December 1998 and routine experiments began in May 1999. This paper describes the technical choices and performance of this beamline, as well as several examples of scientific results obtained during the first 2 years of service.

The beamline uses an X-ray beam with 2 mrad of horizontal divergence emitted from the 0.4 T portion (E_c = 9.6 keV) of the BM30 ESRF bending magnet (beam BM30A). The optics for beam focusing and monochromatization are based on the principle developed previously for beamline BM02/D2AM at the ESRF (Ferrer *et al.*, 1998). The monochromatization and horizontal focus is achieved using a double Si(111) crystal monochromator placed between two cylindrical vertically focusing mirrors. The reflection and diffraction planes of the beam on the mirrors and the monochromator crystals are vertical. This results in a 300 µm FWHM diameter highly monochromated ($\Delta E/E = 1.9 \times 10^{-4}$ FWHM at 1.0 Å) fixed-position beam. The main technical characteristics of the beamline and its optical components are given in Table 1 and Fig. 1.

During construction and since the beginning of normal operation, a large effort was made towards automation of the beamline. The developments achieved in full automation of the optics and the progress made towards the automation of the experiment are described below.

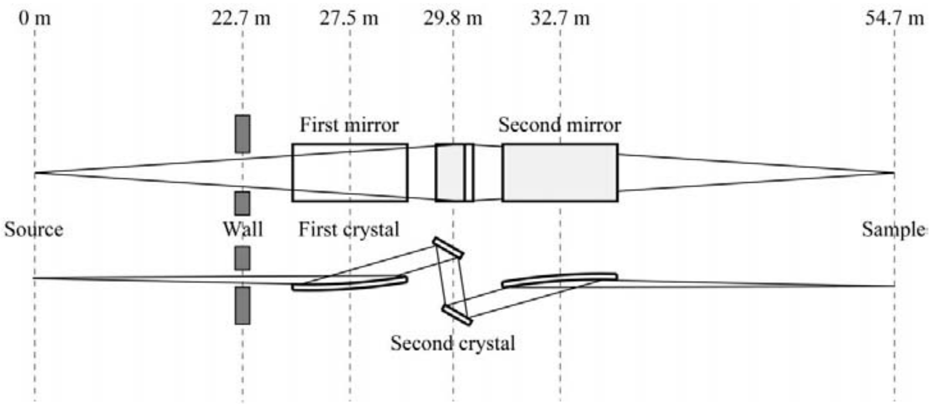

Figure 1
Schematic top and side view of the beamline optics, which consists of a double-crystal monochromator (crystals 1 and 2) placed between two grazing-angle mirrors. The diagram gives the distance to the source (storage ring) of the main components.

Table 1
Parameters of the optics.

Source (0.4 T bending magnet)	
Size (cross-section) (mm^2 FWHM)	0.3 × 0.3
Vertical divergence at λ = 1 Å (mrad FWHM)	0.1
Horizontal divergence (mrad)	2.0
Energy range (keV)	7–25
Mirrors†	
Length (mm)	1300
Usable width (mm)	70
Thickness (mm)	60
R.m.s. roughness (Å)	~3
R.m.s. slope errors ($''$)	<1
Coating	Pt (400 Å)
Bender	2 actuators
Monochromator‡	
Energy resolution at 1.0 Å ($\Delta E/E$)	1.9×10^{-4} FWHM
Reproducibility (eV)	<0.5
General dimensions	
Source–first mirror distance (m)	27.5
Source–monochromator distance (m)	29.8
Source–second mirror distance (m)	32.7
Source–sample distance (m)	54.7

† First mirror: water-cooled silicon monocrystal. Second mirror: Zerodur glass, no cooling. ‡ Crystal 1: Si(111) monocrystal (60 × 60 × 60 mm) cooled with liquid N_2. Crystal 2: Si(111) plate with ribs on the back, installed on a piezoelectric bender.

2. Mirrors

The two mirrors are cylindrically bent grazing-angle mirrors. The function of the curved mirror upstream with respect to the monochromator is to cancel out the vertical divergence of the incoming beam, resulting in an improvement in the energy resolution (see Fig. 2), while at the same time absorbing a fraction of the beam energy (*i.e.* thermal load) falling on the first monochromator crystal. Using *XOP* (Sanchez del Rio & Dejus, 1997), we estimate that 86 W of a total of 140 W delivered with 200 mA in the ESRF ring is absorbed by the first mirror when the beam is optimized at a wavelength of 1.0 Å (the incidence of the beam on the mirror is kept equal to 75% of the cutoff angle of the selected wavelength). The remaining 54 W is mostly absorbed by the first monochromator crystal, with only 0.01 W reaching the sample. The function of the curved mirror downstream is to focus the beam vertically on the sample crystal placed at the centre of the diffractometer. Both mirrors absorb mostly high-energy photons, rejecting higher order harmonics. The two 1.3 m-long Pt-coated mirrors were polished by SESO (Aix-en-Provence, France). They are installed in a bender supported by a rotating table for the selection of the grazing angle. Both the mirror and the bender are located inside a UHV vessel. The cooling system developed for the first mirror (Ferrer *et al.*, unpublished work) consists of two water-cooled copper plates coated with nickel. Those plates are introduced into two cuts machined on each side of the reflecting surface of the first mirror. These cuts are filled with a Ga–In–Sn eutectic to ensure thermal conduction without mechanical coupling. As a consequence of this efficient cooling associated with the use of silicon as bulk material for the mirror itself, no thermal deformation is observed, as was predicted by finite-elements analysis performed for similar mirrors (Roth *et al.*, 1992). The second mirror, located after the monochromator, is geometrically symmetrical with respect to the first one. Without significant thermal load, no water cooling is required and Zerodur glass was chosen as the bulk material. This mirror focuses the beam on the sample located nearly 20 m downstream and, in conjunction with the first mirror, contributes to the harmonic rejection.

3. Monochromator

3.1. Cryogenic cooling of the first crystal in the monochromator

According to the energy resolution of the beamline ($\Delta E/E = 1.9 \times 10^{-4}$ FWHM at 1.0 Å), only a very small fraction of the total emitted photons reaches the sample. Thus, the thermal energy is dissipated between the first mirror for the high-energy photons and the first crystal of the monochromator for the remaining softer photons. This latter part, of the order of 30–80 W, increases with the energy selected in the monochromatic beam (the higher the energy, the smaller the grazing angle of the mirror and therefore the smaller the fraction absorbed by the mirror). The related heat load flows from the beam footprint through the volume of the crystal to the heat exchangers to be evacuated. This heat propagation inevitably establishes a temperature gradient associated with the thermal conductivity of silicon. Consequently, a thermal distortion of the crystal appears, which is detailed as the combination of the bump arising from the thermal expansion perpendicular to the surface and bilayer effects resulting from the expansion parallel to the surface. Using a water-cooling system to thermalize the crystal, the slope error left in the reflecting face spreads the X-ray beam over an angular area

$\Delta\theta$ of the order of magnitude of the Si(111) Darwin width (Hoszowska *et al.*, 2001). The resulting deterioration of the efficiency of the double-crystal monochromator, especially at shorter wavelengths (<1 Å) where the Bragg angle is small, induces a significant loss in intensity. To avoid this problem, the best known solution is the cryogenic refrigeration of the first crystal. Below 125 K, silicon demonstrates interesting thermal properties: a quasi-zero expansion coefficient and a huge thermal conductivity (Touloukian, Kirby *et al.*, 1975; Touloukian, Powell *et al.*, 1975). An efficient liquid-nitrogen (LN_2) closed-loop cooling system has been developed previously at the ESRF to maintain monochromator performance on the highly brilliant insertion-device beamlines (Marot *et al.*, 1992). For such sources, this cooling method is essential to reduce the distortion of the diffracting crystals and thus to maintain a high-intensity throughput of the monochromator.

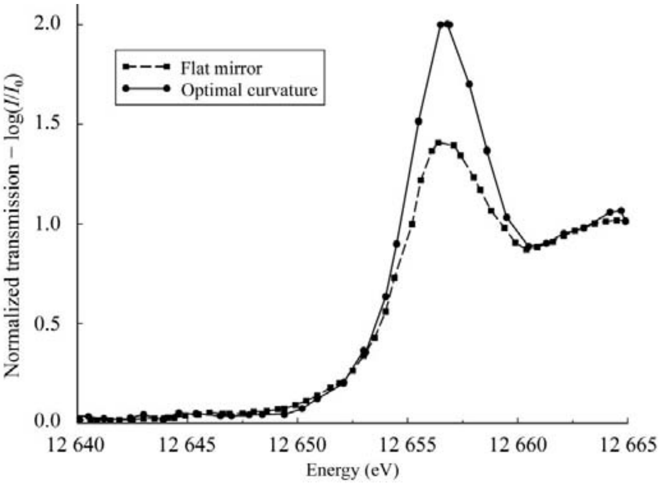

Figure 2
Fluorescence at the absorption *K* edge of Se measured on the beamline: bending the first mirror for collimating the beam improves the energy resolution of the monochromator, as can be seen by the sharpening of the white line.

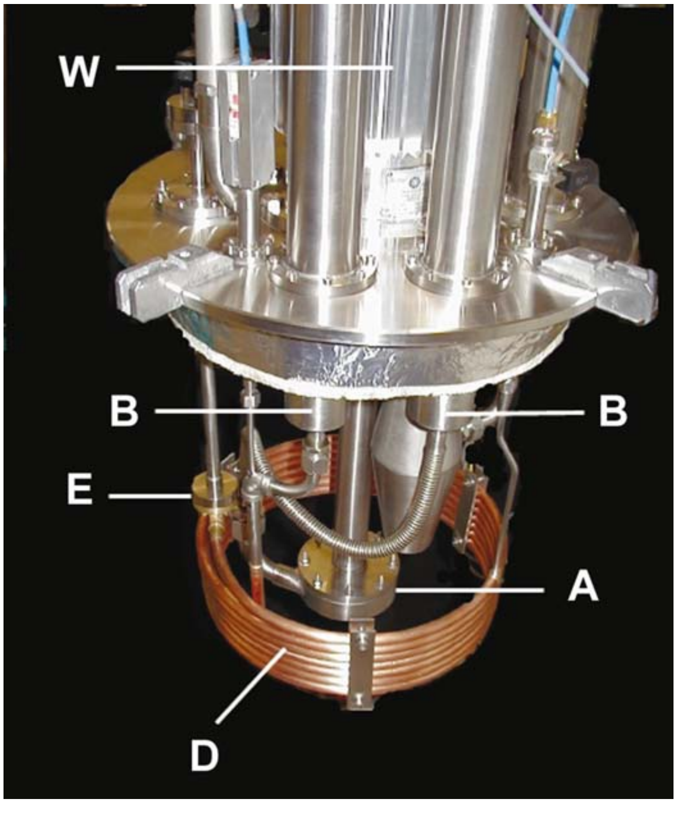

Figure 3
Picture of the main components of the cryogenic system used for the monochromator's first crystal cooling, showing the circulator (A and W), the departure and the return of the LN_2 transfer line (B) terminated by the cooler (D) and the expansion valve (E). [Reprinted with permission from Carpentier *et al.* (2001). Copyright Elsevier Science.]

For simplicity and lower cost, we have devised a new type of LN_2-cooling loop (Fig. 3) based on an open thermodynamic system adapted to the energy dissipation of a bending-magnet X-ray beam (Carpentier *et al.*, 2001). The liquid nitrogen, taken from a cryogenic reservoir at 77 K and atmospheric pressure, is circulated in a heat exchanger in close thermal contact with the Si crystal and then returned to the reservoir. The slightly pressurized cooling fluid (1500 Pa above atmospheric pressure) stores the heat while flowing across the heat exchanger, where it is heated up by a few kelvin. The fluid is then cooled to 77 K by circulating in a long spiral copper tube plunged in the LN_2 reservoir, before returning the LN_2 to the reservoir *via* an adjustable valve which controls the flow. The cooling of the fluid produces a slight boiling of the LN_2 in the reservoir. The heat of the Si crystal is thus indirectly taken away by LN_2 evaporation. Periodically, the reservoir is refilled to replace LN_2 lost by evaporation. The LN_2 circulation is achieved with a cryogenic circulator (BNCP43; Barber & Nichols, USA). The crystal's heat exchanger was manufactured according to the ESRF design (G. Marot & M. Rossat, private communication).

The major difficulty with such a forced convection heat-exchanger system is to avoid the mechanical vibrations that can be produced by the flowing fluid. The resulting crystal angular oscillations may easily reach or exceed the value of the Darwin width. This would lead to a dramatic diminution of the beam intensity by deteriorating the monochromatization efficiency of the monochromator and by producing downstream X-ray beam oscillations at the sample position. Particular attention has been paid to avoid this effect. Firstly, taking into account the power density of the source, it was calculated that a flow rate of about $150\,\mathrm{l\,h^{-1}}$ of pressurized LN_2 at 1500 Pa is suitable to dissipate the bending-magnet heat load without any bubbles forming in the exchanger which would shake the crystal. The heat exchanger was then designed to work under a laminar-flow regime in order to protect the crystal from vibrations produced by turbulence of the fluid. Finally, it was observed that under this regime no vibration is generated by the cryopump impeller in the fluid, the BNCP43 circulator working smoothly with a low rotation speed of 2700 rev $\mathrm{min^{-1}}$ at 1500 Pa and a stability better than 50 Pa.

The efficiency of the system with respect to the thermal distortion of the crystal has been verified experimentally. The rocking curve of the monochromator has been measured at different energies over the complete working range of the beamline (0.7–1.81 Å) and compared with the theoretical double reflectivity computed by *XOP* (Sanchez del Rio & Dejus, 1997) (*i.e.* with the auto-convolution of the Si(111) reflectivity curves). No significant thermal deformation can be detected using the Si(111) reflection as a monitor. The scaled rocking curves of the monochromator are equal at all wavelengths to the theoretical double reflectivity of perfect crystals, as shown in Fig. 4. The absence of thermal distortion of the first crystal is also attested by the behaviour of the image of the beam on a fluorescent screen at the monochromator exit during the tuning of the second crystal with respect to the first crystal. The footprint is as wide as the crystal itself. It does not move appreciably in the vertical direction and the intensity increases uniformly over the whole surface of the trace. As a consequence of this lack of thermal bump, no strong decrease of the intensity of the beamline is observed down to 0.7 Å (see Table 2). This high intensity permits the recording of effective MAD data at the $L_{\rm III}$ absorption edge of uranium (0.722 Å). This constitutes an important feature of the beamline FIP, as uranium derivatives are often efficient derivatives in protein crystallography.

The large thermal conductivity of silicon at 77 K allows the thermal equilibrium steady state of the first crystal to be reached almost immediately after the beginning of irradiation. Thus, achieving thermal equilibrium of the first crystal of the monochromator, after a synchrotron reinjection for instance, is not problematic. Another consequence of the large thermal conductivity is that the temperature increase at the reflecting surface is very small (about 1–2 K as currently observed) and that the crystal temperature is almost insensitive to the heat load. This effect, together with the stability of the LN_2 temperature at 77 K, makes the beam very stable over a long period. The system, directly connected to the ESRF liquid-nitrogen supply and equipped with automatic reservoir filling, is very safe and does not require much more attention than an ordinary water-cooling system. Nevertheless, a complete shutdown and purge of the system has to be carried out every two weeks, in order to eliminate ice trapped in the loop that, after a few weeks of continuous functioning, would disturb the smooth LN_2 circulation. Heating and drying of the whole loop is achieved within 6 h. The automation of the purge process is currently in progress. After restarting the cooling loop, the crystal reaches its steady state at nearly 77 K in 10 min. Nevertheless, it takes a further 5 h to stabilize the temperature of the mechanical holder of the crystal on the monochromator (Fig. 5) in spite of its thermal insulation by zircon (ZrO_2). During that time, a slow drift inducing a progressive detuning of the two crystals occurs, which necessitates frequent re-adjustments.

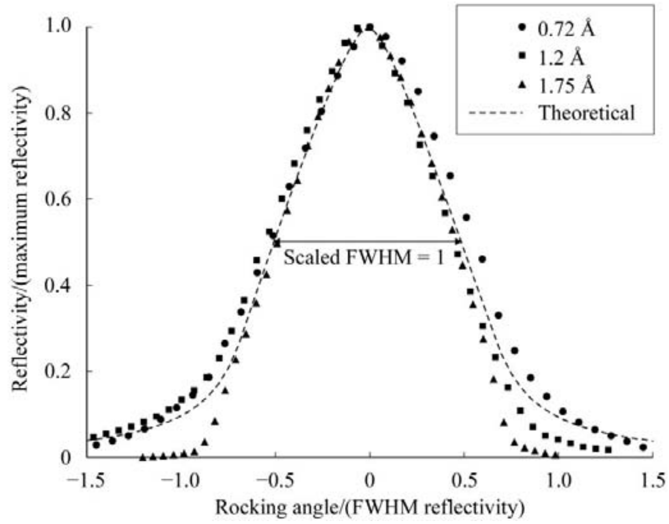

Figure 4
Rocking curves of the monochromator's second crystal at several wavelengths. The maximum is normalized to one and the width is normalized by the value from X-ray dynamical diffraction theory. The measured shapes and widths are very close to those of the theoretical rocking curve, demonstrating the distortion-free surface of the cryo-cooled first crystal. The triangular shape results from the convolution of the almost square Darwin curves of the two crystals.

Table 2
Relative intensity (number of photons per second) at the sample position, measured with an ion chamber located ∼20 cm upstream of the sample position and normalized to the maximum intensity, observed at ∼1.28 Å, compared with the intensity computed with *XOP* (Sanchez del Rio *et al.*, 1997).

Wavelength (Å)	Relative intensity (measured/theoretical)
0.72 (U $L_{\rm III}$ edge)	0.56/0.57
0.92 (Br *K* edge)	0.59/0.76
0.98 (Se *K* edge)	0.68/0.8
1.28 (Zn *K* edge)	1.00/1.00
1.71 (Gd $L_{\rm III}$ edge)	0.16/0.56

This cryogenic cooling system, which was built as a prototype for beamline FIP, has been working successfully there for several years. In the light of all this experience, and based on the comparisons performed on measurements at BM05 at ESRF (Hoszowska *et al.*, 2001), we believe that on bending-magnet beamlines this system is a viable alternative to conventional water cooling.

3.2. Piezoelectric crystal bender

The second crystal in the monochromator is sagittally bent to produce horizontal beam focusing. It is well known that bending a thin plate in one direction parallel to its plane produces a significant anticlastic bending in the perpendicular direction, resulting in an overall saddle-shape deformation of the crystal. This effect can be avoided by using appropriate crystal shapes, which can be either a long crystal bent by application of a uniform couple along both parallel sides (Kushnir *et al.*, 1993) or a crystal with ribs at the back (Sparks & Ice, 1982). In practice, bending can also produce twist and conical deformation of the crystal (Ferrer, 1999). Our bender has been designed for curving a long crystal, *i.e.* a crystal of long thin plate shape with two strong lateral bars on each side. The couple is applied by four piezoelectric actuators which push the crystal on the back of the bars, two on each side, against four coplanar supporting points of the crystal (Fig. 6). The force applied to the crystal by each piezoelectric actuator is controlled by an individual force sensor and stabilized to a fixed value by continuous feedback. The crystal curvature is mainly determined by these applied forces (order of magnitude of 20–50 N) and is therefore very stable and reproducible. The twist of the crystal is eliminated by a motorized micrometric adjustment of the position of two of the supporting points. A possible sigmoidal deformation of the bent crystal is corrected by a proper weighting of the forces of one side with respect to the other. Conical deformation can neither be produced nor be corrected by this bender owing to the lateral bars that maintain the rotation of the crystal edge along the beam direction constant. Attempts to machine an appropriate U-shaped crystal from an Si single-crystal block were ultimately unsuccessful and were consequently abandoned. An alternate system was used instead: a standard back-ribbed Si crystal was glued onto two parallel INVAR bars that were assembled with two 0.6 mm thick silica glass plates glued at both ends onto the INVAR bars by high-vacuum epoxy (Fig. 6). The curvature of the ensemble is mainly controlled by the elasticity of the glass plates. INVAR and silica were chosen as materials since their thermal expansion coefficients are similar to that of Si. The assembly must be heated to 353 K to glue the crystal onto the INVAR with Wood's alloy (50% bismuth, 25% lead, 12.5% tin and 12.5% cadmium). The choice of materials and a carefully controlled decrease in temperature minimize the strain on the glued crystal and prevent conical deformation. The resulting focused beam is about 300 μm in width, instead of the theoretical 100 μm, mostly owing to the reduced curvature on top of the ribs. This behaviour is confirmed when the ribs become visible on the image of a slightly unfocused beam at the sample position.

The bender is installed on a three-axis table for orienting the crystal. The motors, as well as a plate behind the bender, are water cooled in order to eliminate the heat load (Compton scattering from the first crystal and motor power) and therefore ensure a good temperature stability of the crystal. The functioning of the piezoelectric bender and its holder has proven to be excellent in terms of stability and reproducibility. This allows full automatic beamline alignment at any wavelength, as described below, including the optimization of the sagittal focusing of the beam.

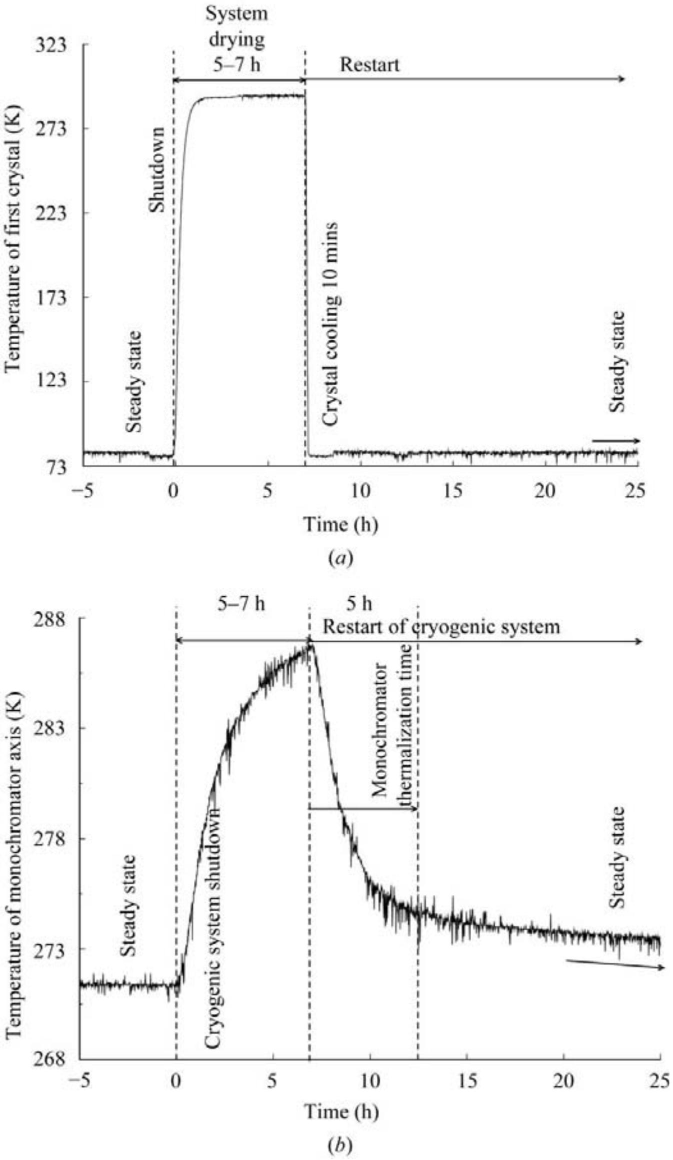

Figure 5
Evolution of the temperature of the crystal and of the mechanics of the monochromator during a shutdown and restart of the cryocooling of the crystal: (*a*) temperature measured directly on the crystal, (*b*) temperature of the shaft of the monochromator on which the cooling crystal holder is fixed. About 5–7 h is required after restarting cryocooling to re-attain the thermal equilibrium of the monochromator.

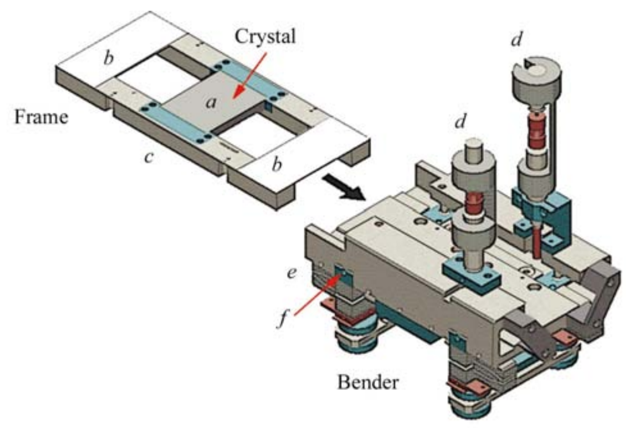

Figure 6
Schematic view of the ribbed crystal *a* on its frame and of the bender. The frame is constituted of two 0.7 mm thick silica glass plates *b* which act as flexion springs, glued with hard epoxy on two rigid INVAR shafts *c*. The crystal is glued in the middle part of the shafts. For producing the curvature, the frame, mounted in the bender, is pushed against four fixed points, the height of two of them being adjusted by a stepper-motor-driven vertical translation *d* by four piezo-actuators *e*. The strength applied by each actuator is controlled by a force sensor *f* located between the actuator and the frame.

4. Automation

4.1. Beamline-control software

The developments listed below were undertaken to increase the automation of the beamline. The aim of this automation is to provide safer working conditions for the users and to increase the throughput and quality of collected data. Developments related to the data collection were achieved with the beamline-control software *nemo* developed by E. Fanchon (unpublished work).

The *nemo* language is interpreted and provides all the functionalities of procedural languages (loops, conditions, function definition *etc.*). The *nemo* interpreter has a C-like syntax and is itself written in ANSI C. It fits into the client–server architecture developed at ESRF: devices are controlled by so-called device servers. These processes run on VME crates under the OS9 operating system and offer a well defined interface to higher level applications. The *nemo* interpreter is one such application: it is a client running on a Unix workstation which sends requests over the local network to the various device servers needed to perform its task.

An emphasis has been put on structured programming to increase the readability, reliability and maintainability of the code: *nemo* implements a typed language with arrays and structures. Structures can contain numerical values, strings, arrays or other structures. Similarly, arrays of any type of data can be defined. Predefined types for basic devices such as motors, timer/counters and analogue-to-digital converters are available. Once a variable of a given type is declared, its type cannot be changed. This is in contrast to languages such as python which allow such changes. Static typing is a constraint but leads to a much more reliable code, especially when scripts are modified by different people over time. Functions represent separate pieces of code: variables declared in the body of a function are local to this function. Global variables can be defined, but must be explicitly imported to be used within a function. Data objects of any type (even functions) can be passed as argument to functions. The type of argument is checked when a function is called. These features allow the design of groups of functions associated with parts of the beamline (monochromator, mirror, slits, monitors, diffractometer). Each part can function autonomously and can be tested as a separate component. Higher level functions implementing experimental protocols such as beamline alignment or data acquisition can be built from the lower level functions. Communication with a separate graphical user interface (*Xnemo*, see below) is implemented with three sockets: one corresponds to the 'in' channel of the interpreter, one to the 'out' channel and the third is used to send control statements from the interpreter to the graphical user interface (GUI). This separation between data and control statements greatly facilitates interaction with the graphical layer. When invoked by the *Xnemo* GUI, the interpreter uses the control socket to send information on the current beamline configuration (list of devices with parameters). No such information is hardwired in the graphical layer. Thus, there are three software layers with clearly defined functionalities: device servers which provide an interface with individual pieces of hardware, the *nemo* interpreter and the graphical user interface. All the actions triggered from the GUI are translated into *nemo* commands. There is no direct communication between the GUI and the device servers.

An interpreted language is well suited to speeding up the development-test cycle. Interpreted scripts are slower to execute, but performance is not an issue for this kind of instrument-control application. Real-time constraints are implemented at the level of device servers.

4.2. Automated alignment of the beamline

Changing the wavelength of the beam implies changing the inclination of the mirrors (to keep an optimal energy filtering), changing the incidence of the crystals of the monochromator, changing the position of these crystals and changing the curvature of the mirrors and the second monochromator crystal. These changes are all made automatically using the values of the actuators determined by interpolation from tabulated values. Once these main beam adjustments have been made, several fine optimizations must be carried out: tuning of the monochromator crystals (adjustment of lattice plane parallelism), centring of the beam on the collimator, adjusting the horizontal focus on the sample position and optimizing the shape of the sagitally bent crystal (Fig. 7). The final operations are made using intensity monitors (an ionization chamber placed before the collimator and a photodiode placed in the beam just behind the sample) and a fluorescent screen for localizing the beam and analyzing its shape. The photodiode and the screen are moved in and out of the beam automatically. All these operations are computerized and do

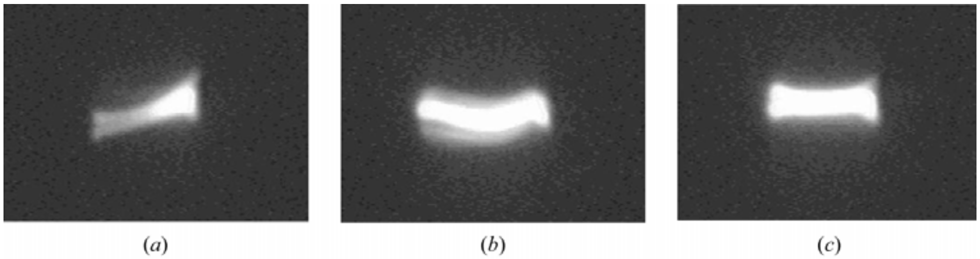
(*a*) (*b*) (*c*)

Figure 7
Typical images of the beam, horizontally focused by bending the second crystal of the monochromator, as observed at about 1 m upstream from the focal point on a fluorescence screen at three steps of the automated beam optimization (the real size of the beam in these pictures is about 1–2 mm). (*a*) Distortion intensity distribution arising from twist of the curved crystal; (*b*) after twist correction, residual asymmetrical intensity distribution arising from a slightly sigmoidal curvature of the crystal; (*c*) after curvature symmetrization, final homogeneous and horizontal beam. All corrections are achieved by changing the parameters of the piezo-actuators adjusting the curvature of the crystal. The parameters are obtained by analyzing these images.

not need any user intervention. Aligning the beam at a given wavelength takes approximately 5–10 min. The majority of alignment time is spent in the optimization scans, although a fast-scan technique is used. Fast scans are achieved at the level of the VME electronics in the following manner: the device which is being scanned (for instance, the second crystal for tuning or the second mirror for beam-height adjustment) is rotated continuously and the counting rate accumulated in the appropriate beam-intensity monitor is copied, at regular intervals of the device rotation, into the channels of a multichannel memory. In this way, a cumulative monitor counting-rate curve is recorded as a function of the device position, which gives the rocking-curve intensity by numerical derivation with respect to the position.

4.3. Automated control of the beam intensity

In normal operation (no beam reinjection, no wavelength change), the beam is very stable. The root-mean-square of intensity fluctuations is as low as 0.5% and is up to 1% during refilling of the cryotank of the monochromator (evaluated by measuring background arising from scattering from air and from the sample on the CCD detector: this is a good evaluation of the beam intensity received by the sample as long as it does not move too much in the beam). However, some events, such as ground motion, may lead to a decrease in intensity. For this reason, retuning the monochromator and recentring the beam on the collimator in order to maximize the intensity on the crystal is triggered automatically each time the average intensity found in the last recorded image is lower than 75% of the highest average intensity in the images recorded since the preceding intensity optimization. This is operated during a short (~2 min) interruption of the data collection.

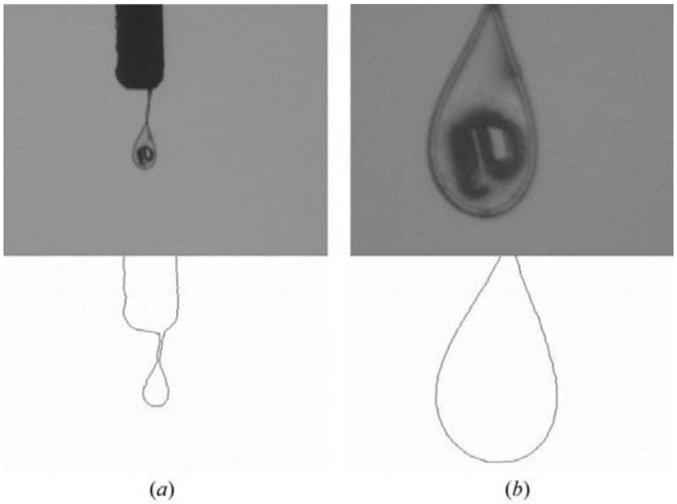

Figure 8
Typical contour extraction performed during automated crystal centring. (*a*) Picture of a loop at low magnification; (*b*) the same picture at highest magnification, after centring at low magnification. The program for contour analysis is able to recognize three kinds of topological objects: cylinder-like (for instance, a capillary), needle-like (for instance, a needle for centre determination) or drop-like (like a loop or a crystal emerging from a loop). If a drop-like object is identified, the centre of mass of the contour of the drop is calculated and its value used for monitoring the automated centring. If the object is too small to be identified as a drop, then it is considered as a needle and the centring is performed according to the coordinates of the tip of the needle. If the program does not find a tip, the object is considered as a cylinder and is aligned with respect to the cylinder axis. Up to now, the program does not analyze the contrast inside the object, which is defined only by its contour.

4.4. Automated accurate calibration of the monochromator near an absorption edge

The measurement of the absorption of the selected filter as a function of the X-ray energy can be automatically carried out with the help of a motorized absorption-filter changer. A band width of ±1% around the absorption-edge energy is scanned and the recorded signal analyzed, giving the exact monochromator rotation-angle value corresponding to the absorption edge. An automated recalibration of the monochromator is then performed by reference to the standard energy of the absorption edge. The accuracy (reproducibility of the calibration) is about ±0.25 eV. This recalibration of the monochromator can be made by the user at any time during data collection. Tests show that it is advisable, in normal operation, to carry out this recalibration at the beginning of each run (about once every two months). This automated recalibration can also be performed by using the fluorescence of the crystal instead of the absorption of a filter.

4.5. Automated crystal mounting and centring

A sample changer is under study. It is based on a commercial robot (Staubli, France) and a dry Dewar currently being developed at EMBL (Grenoble). Standard Hampton loops will be used as much as possible as sample holders.

An algorithm has been developed for the automated alignment of protein crystals mounted in a cryoloop at the centre of the diffractometer. The diffractometer is equipped with a motorized x, y, z goniometer head and a microscope for viewing the crystal with remote-controlled image magnification. In the present stage of development, the algorithm used for image analysis proceeds in three steps. Firstly, the object constituted by loop + crystal + loop thread + pin, as seen in the image of the microscope, is isolated from the image background by external contouring (Fig. 8). The sub-object loop + crystal is then isolated from the rest of the object by analysing of the shape of the contour. Finally, within the area delimited by the external contour of this sub-object, the centres of mass of the brightest and of the darkest areas are determined separately and combined together to obtain an estimate of the position of the centre of the crystal. Our experience shows that this method provides usually a reasonably good estimate of the crystal position, because the brightest and the darkest areas of the loop + crystal sub-object are usually elements of the crystal image alone. The estimated crystal position is then used to shift the crystal towards the centre of the diffractometer. Complete crystal centring obviously requires the repetition of this operation on two crystal orientations differing by 90°. Because of the restricted width of the viewing field of the microscope at the highest magnification, a complete automated centring procedure consists of two steps:

once the crystal has been set on the goniometer head (by the user or, in the future, by a robot), a first centring is performed either at low or at medium magnification and is followed by fine centring at the highest magnification. This operation requires about 3 min, most of it being spent in sample rotations. It will be faster in the future with an upgrade of the diffractometer. The method works on monochromatic images and does not require any special illumination conditions.

4.6. Automated data collection

Dialogue with *nemo* is performed through a GUI, *Xnemo*, derived from *ProDC*, the standard GUI at ESRF (Spruce, unpublished wprk). With this interface, the user can safely (i) manipulate the diffractometer geometry (centring and orientation of the sample, displacement of the detector), (ii) perform and process an energy scan and (iii) prepare and run the data collection. For this last operation, the user can define the mode (single image, monochromatic, SAD, MAD, MAD in inverse-beam mode) and beam controls (automated optimization in case of intensity decrease and optionally at wavelength change) as well as usual parameters. The data collection can then be run completely unattended, as the program takes care of the beam optimization and changes the wavelength automatically. For user information, a continuous plot of the average image intensity, as well as the normalized fluorescence of the sample, is drawn. Any important event occurring during the data collection (change of the wavelength, intensity optimization, any failure, end of the data collection *etc.*) is described in the log file and commented through a loudspeaker. Moreover, it is now possible to prepare a series of data sets using *Xnemo* as an editor and run them sequentially without the user's intervention. For example, a user can prepare and run in a completely unattended mode a sequence of data collections such as

(i) a high-resolution (large 2θ) single-wavelength data collection,

(ii) a medium-resolution inverse-beam mode MAD data collection,

(iii) a short MAD data collection at another crystal orientation (to obtain the blind region) and

(iv) a fast low-resolution data collection.

This possibility of a series of data collections will become essential when a robot is available for sample changing.

4.7. On-line data treatment

The specific parameter and command files required for running the data-reduction programs *HKL* (Otwinowski & Minor, 1997), *MOSFLM* (Leslie, 1990) and *XDS* (Kabsch, 1988) are automatically created by the data-acquisition program at the beginning of each data collection. This allows the user to process and analyze the data immediately with only very little and simple file editing. The user simply has to input the space group, the mosaicity and the integration box parameters. Some operations, such as orienting the crystal, looking for the best data-collection strategy or translating the final reduced data in various popular formats, can be performed in html-based GUIs.

Alternatively, a script is now available to perform these tasks completely automatically (Ferrer, 2001). This script successively performs

(i) a peak search with *MARPEAKS* from MAR Research (Klein, unpublished work),

(ii) indexing with *DENZO* (*HKL* package),

(iii) analysis of indexing scores for the evaluation of the space group,

(iv) evaluation of the best strategy,

(v) estimation of possible pre-orientation compatible with the diffractometer,

(vi) integration of frames on-the-fly,

(vii) several cycles of scaling with *SCALEPACK* (*HKL* package) until convergence of refined parameters,

(viii) analysis of systematic extinctions,

(ix) computation of structure factors with *TRUNCATE* (*CCP*4 package; Collaborative Computational Project, Number 4, 1994),

(x) if required, the evaluation of the anomalous signal and

(xi) the calculation of the anomalous Patterson map.

All required parameters, such as the mosaicity, the integration box size, the intensity and resolution thresholds as well as the number of residues per asymmetric unit are automatically evaluated. This development was made necessary by the short time now required for a complete data collection (typically 1 h for 120° data collection, with 15 s exposure per degree). Moreover, as integration can be performed during data collection, users can obtain statistics on scaled data and a first anomalous map just a few minutes after the end of the data collection, providing the necessary information to decide if further data collection is needed. All these procedures help to minimize dead time during data collection.

In each data set, an index file, when opened with an html browser, gives direct access to data collection and data-processing log files as well as a picture of the crystal and the result of processing performed either manually (with the html GUI) or automatically.

5. Scientific results

Most new structures are now solved by making use of anomalous signal. It is one of the many reasons why synchrotron radiation is so important for protein crystallography. This is shown by the increasing number of users wanting to solve structures with SAD/MAD experiments. Owing to the fast (10 min) and automated procedures for changing the wavelength and optimizing the beam on FIP, several heavy atoms can be tested in a few hours. The collection of a complete MAD data set on FIP at three wavelengths in space group *P*1 on a typical 100–300 µm-long crystal requires approximately 8 h for a 15 s exposure per 1° oscillation (compared with 3–4 h for the same experiment on a very intense undulator beamline at ESRF). The technical feasibility of experiments, considering the protein size and resolution limit, is continuously re-evaluated as more and more technically challenging structures are solved, as illustrated by these few recent examples:

(i) molecular-replacement structure of crystals with a unit-cell parameter as large as 460 Å (Budayova-Spano *et al.*, 2002),

(ii) MAD structure obtained on crystals with a solvent content of as high as 83% (Richard *et al.*, 2002),

(iii) 1.1 Å resolution data set collected on a crystal with 84 kDa per asymmetric unit (Borel *et al.*, unpublished work). A short selection of published results obtained on FIP corresponding to particularly challenging biological projects is given below.

5.1. Transhydrogenase complex (Buckley *et al.*, 2000)

The selenomethionine-labelled protein crystallizes in space group $P2_1$, with unit-cell parameters a = 65.9, b = 116.6, c = 102.0 Å, β = 104.2°, and has four polypeptide chains in the asymmetric unit. Data were collected to 2.0 Å at three wavelengths (0.9796, 0.9794 and 0.9686 Å) corresponding to the Se K-edge f' minimum, f'' maximum and high-energy distant positions, as determined from a fluorescence scan of the crystal. The data were processed and merged using *DENZO*/*SCALEPACK* (Otwinowski & Minor, 1997) (Table 3). The anomalous signal was found to extend to 2.5 Å. The SeMet substructure was solved using the 'half-baked' approach as implemented in the program *SHELXC* (Sheldrick, 1990). 52 sites were found and refined using *MLPHARE* (Otwinowski, 1991) using the λ_3 data as the native data set. Solvent flattening was applied using *DM* (Cowtan, 1994) and an initial model was built into the MAD-phased map at 2.5 Å. Rounds of refinement and rebuilding resulted in a final model of 12 741 atoms, including 1459 solvent atoms, with R = 0.21 and $R_{\rm free}$ = 0.26. In the final model, there are no non-glycine Ramachandran outliers, 92.6% of the residues are in the most favoured conformation and 51 of the initial 52 Se sites corresponded to actual SeMet positions.

5.2. Human nuclear cap binding complex (Mazza *et al.*, 2001)

Crystals of cap binding complex grow in space group $P2_12_12_1$, with unit-cell parameters a = 75.87, b = 162.88, c = 304.34 Å and three complexes per asymmetric unit. By incorporation of 19 SeMet per complex, 57 Se atoms were expected in the asymmetric unit. The statistics of the 3 Å resolution MAD data collection are given in Table 4. Using peak-wavelength structure factors only, 57 out of 57 Se sites of were found by *SHELX* (Sheldrick, 1990) from their anomalous differences. These structure factors were phased by *MLPHARE* (Otwinowski, 1991). Phases were then extended to 2 Å by solvent flattening and threefold NCS with *DM* (Cowtan, 1994), using 2 Å native data collected at ID14-EH2 at the ESRF. Automatic model building with *WARP* (Perrakis *et al.*, 1999) allowed the placement of 2015 out of 2500 residues with their side chains.

Table 3
Data-collection statistics on transhydrogenase complex (Buckley *et al.*, 2000).

Values for unique reflections, completeness and redundancy are given without and (in parentheses) after merging Bijvoet pairs. For $I/\sigma(I)$ and $R_{\rm sym}$ the values in parentheses are for data in the highest resolution shell.

Data set	λ_1 (0.9796 Å)	λ_2 (0.9794 Å)	λ_3 (0.9686 Å)
$d_{\rm min}$ (Å)	2.0	2.0	2.0
No. of unique reflections	165625 (93731)	165837 (93853)	184728 (99140)
Completeness (%)	78.3 (87.5)	78.4 (87.7)	87.4 (92.7)
Redundancy	1.58 (2.80)	1.62 (2.87)	1.71 (3.22)
$I/\sigma(I)$	13.38 (2.24)	12.86 (2.06)	14.06 (2.50)
$R_{\rm sym}$† (%)	4.4 (27.1)	4.7 (29.5)	4.3 (27.1)

† $R_{\rm sym} = \sum_j |\langle I\rangle - I_j| / \sum\langle I\rangle$, where I_j is the intensity of the jth reflection and $\langle I\rangle$ is the average intensity.

Table 4
Data-collection statistics on human nuclear cap binding complex (Mazza *et al.*, 2001).

Data set	Peak	Inflection	Remote
X-ray wavelength (Å)	0.9794	0.9796	0.97
Exposure/image	6 s/0.3°	6 s/0.3°	6 s/0.3°
No. of images	639	621	624
Resolution (Å)	50–3.0	50–3.0	50–3.0
Unique reflections	76346	76366	76235
Average redundancy	7.8	7.3	7.1
Completeness (%) (anomalous)	99.7 (99.4)	99.6 (99.5)	99.6 (98.8)
$R_{\rm merge}$ (highest bin)	0.049 (0.111)	0.046 (0.115)	0.055 (0.145)

5.3. Extracellular domain of the common β-subunit of the human GM-CSF, IL-3 and IL-5 receptors (Carr *et al.*, 2001)

The receptor systems for the haematopoietic cytokines GM-CSF, IL-3 and IL-5 (related cytokines involved in the regulation of hematopoiesis and inflammation) consist of ligand-specific α-receptor subunits that play an essential role in the activation of the shared βc subunit, the major signalling entity.

The structure of the complete βc extracellular domain was determined to a resolution limit of 3.0 Å. The crystals obtained belong to the space group $R3$, with unit-cell parameters a = 185.7, c = 103.3 Å, and contain two molecules in the asymmetric unit. The structure was determined by multiple isomorphous replacement with anomalous scattering (MIRAS) using six cysteine substitution mutants for the preparation of heavy-atom derivatives. Data were collected at a wavelength of 1.0085 Å. The structure was refined to an $R_{\rm cryst}$ of 0.267 and an $R_{\rm free}$ of 0.304 for data extending to 3.0 Å. The structure is a dimer of two identical subunits and comprises 408 out of 419 residues in each chain with glycosylation at N34 and N167. Residues 259–266 and 417–419 were disordered in the crystal and excluded from structural analysis.

6. Conclusions

Thr CRG-FIP beamline was built to deliver the best X-ray beam from a bending magnet in a wide energy range for MAD/SAD experiments. The goal was achieved using optics where almost any faults can be corrected by actuators or prevented by efficient cooling devices. The efforts for the automation of the optics and the experiment make it very user-friendly and the beamline can be used even by novice crystallographers. Difficult structures already solved on FIP demonstrate that such a beamline using a bending magnet as a source can be used for challenging projects.

Construction of CRG-FIP beamline was funded by the Commissariat à l'Energie Atomique (CEA), the Centre National de la Recherche Scientifique (CNRS), the Région Rhône-Alpes, the Ministère de l'Education Nationale and the Fond National pour la Recherche Scientifique (FNRS, Belgium). Operation of the beamline is funded by CEA, CNRS and FNRS. People involved in the construction, other than the authors, are Dominique Grand (general layout, CNRS/SERAS), Philippe Jeantet (mechanical study, CNRS/SERAS), Lionel Mallet (machining, EMBL), Jean-Paul Roux (head of the design department, CNRS/SERAS) and Pierre Taunier (general layout, CNRS/SERAS).

References

Buckley, P. A., Jackson, J. B., Schneider, T., White, S. A., Rice, D. W. & Baker, P. J. (2000). *Structure*, **8**, 809–815.

Budayova-Spano, M., Lacroix, M., Thielens, N. M., Arlaud, G. J., Fontecilla, J. C. & Gaboriaud, C. (2002). *EMBO J.* **21**, 1–9.

Carpentier, P., Rossat, M., Charrault, P., Joly, J., Pirocchi, M., Ferrer, J.-L., Kaïkati, O. & Roth, M. (2001). *Nucl. Instrum. Methods A*, **456**, 163–176.

Carr, P. D., Gustin, S. E., Church, A. P., Murphy, J. M., Ford, S. C., Mann, D. A., Woltring, D. M., Walker, I., Ollis, D. L. & Young, I. G. (2001). *Cell*, **104**, 291–300.

Collaborative Computational Project, Number 4 (1994). *Acta Cryst.* D**50**, 760–763.

Cowtan, K. (1994). *Jnt CCP4/ESF–EACBM Newsl. Protein Crystallogr.* **31**, 34–38.

Ferrer, J.-L. (1999). *Nucl. Instrum. Methods Phys. Res. A*, **431**, 224–233.

Ferrer, J.-L. (2001). *Acta Cryst.* D**57**, 1752–1753.

Ferrer, J.-L., Simon, J.-P., Berar, J.-F., Caillot, B., Fanchon, E., Kaïkati, O., Arnaud, S., Guidotti, M., Pirocchi, M. & Roth, M. (1998). *J. Synchrotron Rad.* **5**, 1346–1356.

Hoszowska, J., Mocella, V., Zhang, L., Migliore, J.-S., Freund, A. K. & Ferrero, C. (2001). *Nucl. Instrum. Methods Phys. Res. A*, **467–468**, 631–634.

Kabsch, W. (1988). *J. Appl. Cryst.* **21**, 67–71.

Kushnir, V. I., Quintana, J. P. & Georgopoulos, P. (1993). *Nucl. Instrum. Methods Phys. Res. A*, **328**, 588–591.

Leslie, A. G. W. (1990). *Crystallographic Computing.* Oxford University Press.

Marot, G., Rossat, M., Freund, A., Joksch, S., Kawata, H., Zhang, L., Ziegler, E., Berman, L., Chapman, D., Hastings, J. B. & Lorocci, M. (1992). *Rev. Sci. Instrum.* **63**, 477–480.

Mazza, C., Ohno, M., Segref, A., Mattaj, I. W. & Cusack, S. (2001). *Mol. Cell*, **8**, 383–396.

Otwinowski, Z. (1991). *Proceedings of the CCP4 Study Weekend. Isomorphous Scattering and Anomalous Replacement*, edited by W. Wolf, P. R. Evans & A. G. W. Leslie, pp. 80–86. Warrington: Daresbury Laboratory.

Otwinowski, Z. & Minor, W. (1997). *Methods Enzymol.* **276**, 307–326.

Perrakis, A., Morris, R. M. & Lamzin, V. S. (1999). *Nature Struct. Biol.* **6**, 458–463.

Richard, S. B., Ferrer, J.-L., Bowman, M. E., Lillo, A. M., Tetzlaff, C. N, Cane, D. E. & Noel, J. P. (2002). In the press.

Roth, M., Ferrer, J.-L., Simon, J.-P. & Geissler, E. (1992). *Rev. Sci. Instrum.* **63**, 1043–1046.

Sanchez del Rio, M. & Dejus, R. J. (1997). *Proc. SPIE*, **3152**, 14.

Sheldrick, G. M. (1990). *Acta Cryst.* A**46**, 467–473.

Sparks, C. J. & Ice, G. E. Jr (1982). *Nucl. Instrum. Methods*, **194**, 73–78.

Touloukian, Y. S., Kirby, R. K., Taylor, R. E. & Lee, T. Y. R. (1975). *Thermophysical Properties of Matter*, Vol. 13, *Thermal Expansion of Non-metallic Solids.* New York: IFI/Plenum Press.

Touloukian, Y. S., Powell, R. W., Ho, C. Y. & Klemens, P. G. (1975). *Thermophysical Properties of Matter*, Vol. 1, *Thermal Conductvity of Metallic Elements and Alloys.* New York: IFI/Plenum Press.